Spectroscopic Identification of Disordered Molecular Cations in Defect Perovskite-like A*Ln*$(HCO_2)(C_2O_4)_{1.5}$ (*Ln* = Tb-Er) Phases

Lydia G. Burley,[a] Anant Kumar Srivastava,[a,b] Svemir Rudić[c] and Paul J. Saines*[a]

[a] Miss L. G. Burley, Dr A. K. Srivastava and Dr P. J. Saines
School of Physical Sciences
University of Kent
Canterbury, CT2 7NH, UK
Homepage URL: https://research.kent.ac.uk/frameworks/
E-mail: P.Saines@kent.ac.uk
[b] Dr A. K. Srivastava
Department of Materials Engineering
Indian Institute of Science (IISc)
Bangalore-560012, Karnataka, India
[c] Dr Svemir Rudić
ISIS Neutron and Muon Source
STFC Rutherford Appleton Laboratory
Chilton, Didcot, OX11 0QX, UK

Supporting information for this article is given via a link at the end of the document.

Abstract: This work reports a new series of A*Ln*$(HCO_2)(C_2O_4)_{1.5}$ (A = $[(CH_3)_2NH_2]^+$ and Ln^{3+} = Tb^{3+}-Er^{3+}) compounds made solvothermally. These *Cmce* phases combine monovalent and divalent ligands, which enables a scarce combination of A^+ and B^{3+} cations in a hybrid perovskite-like compound. The ratio of ligands leads to ordered anion vacancies, which alternate with oxalate linkers along the *c*-axis. The A-site cations are disordered and cannot be identified crystallographically, likely a result of the larger pores of these frameworks compared to the recently reported AEr$(HCO_2)_2(C_2O_4)$ phases. Neutron and infrared spectroscopy, supported by elemental composition, enables these cations to be identified as $[(CH_3)_2NH_2]^+$ molecules. Magnetic property measurements suggest these materials have weak antiferromagnetic interactions but remain paramagnetic to 1.8 K.

Introduction

Perovskites have long attracted attention as functional materials due to the fascinating properties they can exhibit including magnetism, electronic and ionic conductivity, ferroelectricity and catalysis.[1–5] Perovskites adopt the ABX_3 stoichiometry in which the A-site cations are large and occupy the space in between the corner-sharing framework of smaller B-site cations linked by anions. The high degree of chemical flexibility exhibited by inorganic perovskites, as seen by their ability to accommodate a wide range of elements across the periodic table, plays a key role in their array of useful properties. This is enabled by the variety of cations with different charges they can contain e.g. A^+/B^{5+}, A^{2+}/B^{4+} & A^{3+}/B^{3+} are all common in perovskite oxides.[5] The flexibility of perovskite related phases is further enhanced by the tolerance of this family to a range of different types of defects, giving rise to structures in which cations and anions are absent in a random or ordered fashion. Well known examples of perovskite-like structures with ordered anion vacancies include the brownmillerite structure, adopted by $A_2Fe_2O_5$ phases in which there are alternating sheets of octahedral and tetrahedral cations, $LaNiO_{2.5}$, where square planar and octahedral B-site cations alternate, and $A_2Mn_2O_5$ phases, where all B-site cations are square pyramidal.[5] Perovskite variants with cation vacancies most commonly do so on the A-site, with alternating layers with lower and higher occupancy observed or, ultimately, the ReO_3 structure in which all A-site cations are absent.[5–7]

In recent years hybrid perovskites that combine inorganic and organic building blocks have attracted significant interest, firstly in the $AB(HCO_2)_3$ phases, which have been studied for their potential as ferroelectrics and multiferroics,[8–11] and, dramatically, in the case of the halide hybrid perovskites related to $[(CH_3)_2NH_2]PbI_3$ that are promising next generation photovoltaics.[12–14] Hybrid perovskites have shown tremendous chemical flexibility via incorporating a wide variety of molecular A and X site ions;[8,11,15–18] the almost complete dominance of monovalent anions, however, has restricted hybrid perovskites to featuring A^+ and B^{2+} cations with the incorporation of B^{3+} cations limited to either double perovskite structures with a 50:50 combination of B^+ and B^{3+} cations or cases with a neutral A-site species, whose retention is not required for charge balance.[8,14,19–21] Recently it has been shown that divalent oxalate ligands can be incorporated into hybrid perovskite-like structures. This was first observed in the perovzalates, which adopt A-site defective $A(Li_3Fe)(C_2O_4)_3$ phases that contain a mixture of inorganic A^+ and, in a 75:25 ratio, B^+ and B^{2+} cations.[22–25] These include $KLi_3Fe(C_2O_4)_3$, which has shown potential as a cathode material for K-ion batteries.[24] Following from this we have reported the AEr$(HCO_2)_2(C_2O_4)$ (A is $[(CH_3)_2NH_2]^+$ or $[(NH_2)_3C]^+$ and *Ln* is a lanthanide) phases, which contain solely A^+ and B^{3+} cations for the first time in a hybrid perovskite structure.[26] Interestingly, the bidentate oxalate ligands in the AEr$(HCO_2)_2(C_2O_4)$ phases feature square antiprismatic LnO_8 cations, deviating from the typical octahedral B-site cation geometry. Critically they still retain a hybrid perovskite structure in which each polyhedra is connected to six neighbours in a *pcu* topology.[27,28] They therefore provide a platform for tuning the ratio of the monovalent and divalent ligands in perovskite-like structures.

There has also been considerable interest in tailoring the properties of hybrid perovskites by introducing vacancies. Hybrid perovskites with A-site vacancies have been explored, including materials in which all A-site cations have been removed to give ReO_3 networks.[29] Amongst the hybrid halide perovskites inclusion of a diamine has been shown to lead to random vacancies on the B and X-sites, which supresses undesirable ion diffusion.[30,31] Vacancy ordered double hybrid perovskites are also known, adopting the K_2PtCl_6-type structure in which half the B-sites are vacant in an ordered fashion.[32,33] Despite this interest in defects there are scarce studies on hybrid perovskite phases with ordered anion vacancies.

Following from our recent results on the $AEr(HCO_2)_2(C_2O_4)$ compounds[26] we have explored the way in which related materials can be altered by changing the ratio of the formate and oxalate linkers in them. In doing so we have created a family of $ALn(HCO_2)(C_2O_4)_{1.5}$ (where *Ln* = Tb, Dy, Ho or Er) compounds with orthorhombic symmetry. These hybrid compounds have a perovskite-like structure but each LnO_8 polyhedra have a missing linker such that they are only connected to five neighbouring polyhedra. While examination of the structure of these materials initially suggests they adopt a ReO_3-like structure, because the A-cation needed for charge balance cannot be located crystallographically, it is ultimately determined that A = $[(CH_3)_2NH_2]^+$ using neutron and infrared spectroscopy, supported by elemental analysis. The A-site cation disorder is likely due to the larger channels in this family compared to related materials. We also probe the magnetic properties in these compounds showing these are consistent with antiferromagnetic coupling.

Results and Discussion

Crystal Structure

The compounds in this work were found to adopt *Cmce* orthorhombic symmetry between 100 K and ambient temperature (see Table S1 for crystallographic information). In the structures determined in this study only the anionic $[Ln(HCO_2)(C_2O_4)_{1.5}]^-$ framework could be resolved, with the cations responsible for charge balance unidentifiable from crystallographic data. There was a lack of any significant residual electron density peaks in Fourier maps, which can result from extensive structural disorder, consistent with the contents of the pores being spatially disordered. The electron density present in the pores were therefore accounted for using the SQUEEZE programme,[34] which yielded between 264 and 339 electrons per unit cell. This is more than adequate for the 216 electrons per unit cell that would be required for $[(CH_3)_2NH_2]^+$ to be present in the pores of the material, which as discussed in the following section is the most likely route by which charge balance may be maintained. The asymmetric unit of these materials contains one lanthanide site, two half oxalate ligands and a formate linker; with the sole exception of those in one of the oxalate ligands the atoms occupy a special position on a mirror plane leading them to have half the occupancy of the general position (see Figure S1).

As in the related $AEr(HCO_2)_2(C_2O_4)$ phases[26] the lanthanide cations adopt an eight-coordinate distorted square antiprismatic geometry, in the $ALn(HCO_2)(C_2O_4)_{1.5}$ phases they are bound to an oxygen atom from two formate linkers and six oxygen atoms from three oxalate linkers, with the bidentate oxalate linker binding through one atom from both carboxylate groups (see Table S2 and S3 for selected bond distances and angles).The difference between the shortest and longest *Ln*-O bonds for each structure varies between 0.08-0.11 Å across the series with, for example, those in $AEr(HCO_2)(C_2O_4)_{1.5}$ varying between 2.266(9) and 2.373(7) Å. The lanthanide cations are confirmed to be trivalent by bond valence sum calculations,

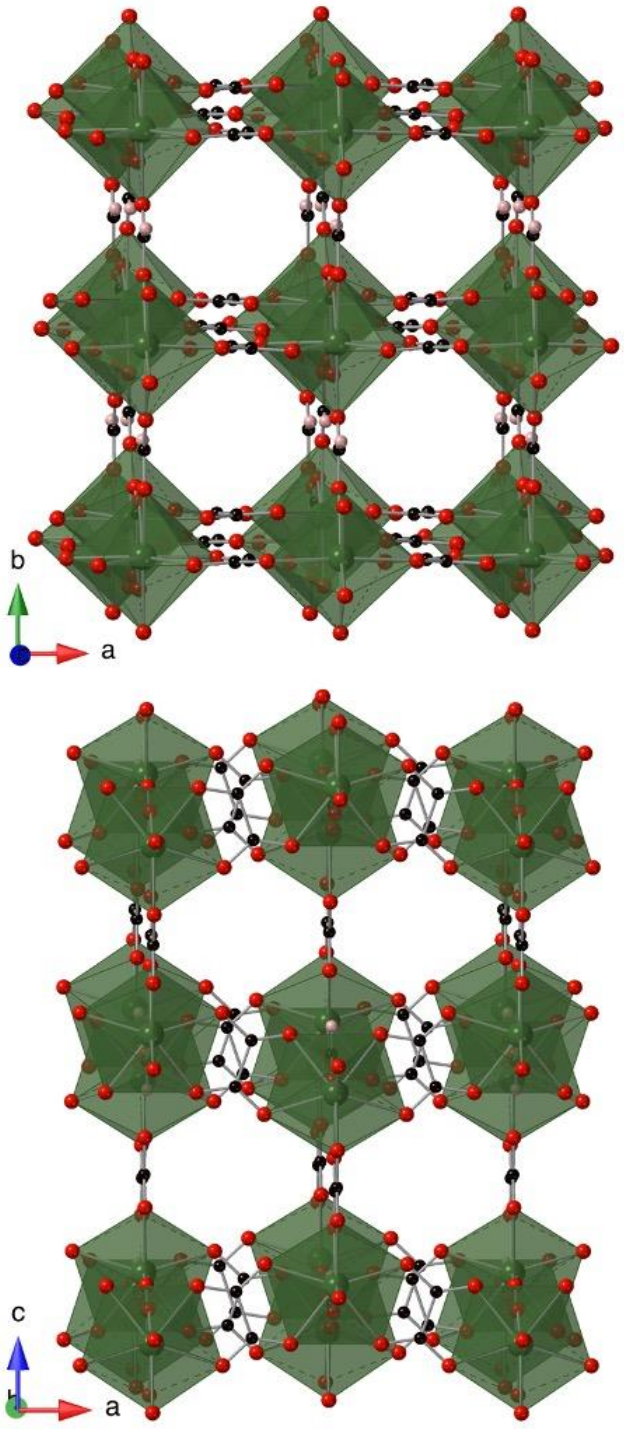

Figure 1. Crystal structure of $AEr(HCO_2)(C_2O_4)_{1.5}$ with ErO_8 polyhedra shown in green and carbon, oxygen and hydrogen atoms shown as black, red and pink spheres, respectively. The A-site needed for charge balance cannot be identified crystallographically.

which vary between 3.07 and 3.24 across the series when calculated using the values of Trzesowska *et al.*[35] for metal-organic compounds. The oxalate and formate ligands connect the LnO_8 polyhedra to five neighbours (see Figure 1). The formate ligands provide the connectivity along the *b*-axis while the oxalates whose atoms occupy the general and special position provide connectivity along the *a*-axis and *c*-axis, respectively; this leads to oxalate linkers alternating with vacancies along the *c*-axis with polyhedra displacing towards the oxalate ligands in this direction. The LnO_8 square antiprism orientation rotates 180° from their neighbours along each axis. The ligand vacancies lead to the $ALn(HCO_2)(C_2O_4)_{1.5}$ phases adopting *sqp* topology rather than the *pcu* structure of stoichiometric ABX_3 perovskites, including the related $AEr(HCO_2)_2(C_2O_4)$ compounds.[26–28] The resemblance of the $ALn(HCO_2)(C_2O_4)_{1.5}$ phases to defect perovskites is emphasised if the midpoint of the two oxygen atoms from each oxalate linker is taken when considering the geometry of the Er node; these then resemble a distorted square pyramidal node as seen in $A_2Mn_2O_5$ defect perovskites,[5] although the oxides adopt *bnn* topology because differences in arrangements of their vacancies.[27,28] In the $ALn(HCO_2)(C_2O_4)_{1.5}$ phases each oxalate connecting polyhedra along the *c*-axis also has vacancies of the nearest neighbour equivalent linkers within the *ab* plane. This leads to the oxalate on the special positions and the vacancies in the structure being arranged in what can be thought of as being a rock salt-like pattern.

A-site Cation Identification

Given the synthetic conditions used to make this family of compounds there are three straightforward ways that charge balance for the anionic framework can be achieved. The first is protonation of one of the carboxylate groups in the formula unit, although this is made less likely by all of the oxygen atoms in these coordinating to lanthanides. The second is hydronium in the pores of the framework, enabled by the presence of water in the reaction mixture. The third is the inclusion of dimethylammonium in the framework pores, which can form from the decomposition of dimethylformamide in cases where none is present as a reagent. Powder X-ray diffraction indicates the bulk materials to be close to pure $ALn(HCO_2)(C_2O_4)_{1.5}$ samples, with only trace peaks from unknown impurities (see Figure S2-5). This enabled the use of elemental microanalysis as an initial method for distinguishing between these three possibilities, since it showed the clear presence of N in these materials, at a % consistent with the presence of $[(CH_3)_2NH_2]^+$ (see Table 1 for values). Furthermore the % H and % C determined are close to the values expected for $[(CH_3)_2NH_2)]Ln(HCO_2)(C_2O_4)_{1.5}$, although the % C values for the Dy and Ho phases are slightly too high, which may suggest the presence of a small amount of a carbon rich impurity in these samples.

A combination of inelastic neutron scattering (INS) and infrared spectroscopy was utilised to clearly identify $[(CH_3)_2NH_2)]^+$ in these frameworks. Infrared spectra found these compounds had a broad peak at 3090 cm^{-1}, consistent with N-H stretching vibrations and 2800-2950 cm^{-1} suggestive of C-H stretching vibrations (see Figure 2). Sharper features are also seen at 1350-1480 cm^{-1} and 980-1060 cm^{-1}, consistent with the range in which C-H bending modes and C-N stretching modes are observed. Intense peaks are also observed around 1590 cm^{-1}, 1310 cm^{-1} and 790 cm^{-1}, which are consistent with C-O stretching and bending modes. Comparison of these spectra to that of $Ln(HCO_2)_3$[36] and $Ln_2(C_2O_4)_3{\cdot}10H_2O$[37] confirms that only the peaks assigned to the C-O and C-H stretching and bending modes would be due to the anionic framework. The remaining peaks likely arise from the $[(CH_3)_2NH_2)]^+$ in the framework pores with the C-N modes being most characteristic of this.

Table 1. Elemental microanalysis of $ALn(HCO_2)(C_2O_4)_{1.5}$ samples.

Lanthanide	Calculated for A = $[(CH_3)_2NH_2]$+	Experimentally Observed
Tb	18.86 % C, 2.37 % H, 3.66 % N	18.96 % C, 2.54 % H, 3.52 % N
Dy	18.69 % C, 2.37 % H, 3.63 % N	19.29 % C, 2.50 % H, 3.69 % N
Ho	18.57 % C, 2.34 % H, 3.61 % N	19.26 % C, 2.49 % H, 3.76 % N
Er	18.45 % C, 2.32 % H, 3.59 % N	18.64 % C, 2.36 % H, 3.64 % N

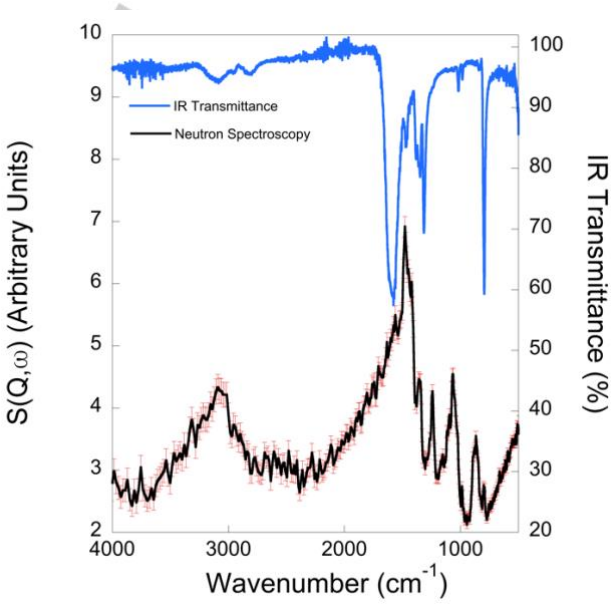

Figure 2. Plot of infrared transmittance and neutron spectra of $AEr(HCO_2)(C_2O_4)_{1.5}$ as a function of wavenumber. The standard deviations in INS intensity are indicated by red markers.

To confirm the presence of $[(CH_3)_2NH_2)]^+$ in the pores of these materials a neutron spectra of $AEr(HCO_2)(C_2O_4)_{1.5}$ was measured due to its far greater sensitivity to the modes involving the motion of hydrogen atoms (see Figure 2 for spectra); such vibrations are the majority of the $[(CH_3)_2NH_2)]^+$ organic cation but are restricted in the framework to C-H stretches from the formate linker. The peaks observed were compared with a simulation of those from an isolated $[(CH_3)_2NH_2]^+$ cation carried out using the programme CrystalMaker X,[38] using a model generated using a hybrid Monte Carlo and least squares optimisation based on Force Field calculations parameterised by Molecular Mechanics 3,[39,40] Williams[41] and Universal Force Field potentials.[42] This comparison confirmed the assignment of the broad peak centred

at 3075 cm^{-1} to a N-H stretching mode and sharp peaks at 1480 cm^{-1} and 1247 cm^{-1} to C-H bends. Peaks at 1358 cm^{-1} and 875 cm^{-1} were assigned to N-H bending modes, noting that these were lowered from calculated modes at 1416 cm^{-1} and 919 cm^{-1} likely due to hydrogen bonding of these functional groups within the framework. It should also be noted that the simulations suggest both C-H and N-H bending modes do not involve pure motion of the assigned functional group but, instead, typically involve a smaller motion of the other. The only two peaks observed above 500 cm^{-1} that could not be assigned by comparison with the simulations were at 1070 cm^{-1}, which may correspond to a C-H bending of the formate linker, and a weak feature at 796 cm^{-1}, which coincides with the O-C-O bending mode observed in the infrared spectra and may be still detected due to some induced motion of the C-H group of the formate. No attempt was made to interpret low energy features below 500 cm^{-1} as these modes often involve concerted motion of the structure. Such modes cannot be simulated with the simple approach used here and would be challenging for more complex calculations due to the uncertain location of the $[(CH_3)_2NH_2)]^+$ in the framework pores.

The presence of $[(CH_3)_2NH_2)]^+$ in the framework channels makes the A*Ln*$(HCO_2)(C_2O_4)_{1.5}$ series the second group of hybrid perovskite-like phases to contain A^+ and B^{3+} cations, alongside the AEr$(HCO_2)(C_2O_4)_{1.5}$ phases.[26] The inclusion of $[(CH_3)_2NH_2]^+$ A-site cations is consistent with the use of $[(CH_3)_2NH_2]^+$ as a reagent, rather than simply relying on this forming from the decomposition of solvent, improving the yields obtained from the reaction. The cause of the extensive disorder of these $[(CH_3)_2NH_2]^+$ cations is likely due to the large fraction of the channels in the structure. Calculations indicate 42-43 % void space within the anionic framework using the programme Mercury[43] and a 1.2 Å probe radius *c.f.* to 26-27 % for the closely related $[(CH_3)_2NH_2)]$Er$(HCO_2)_2(C_2O_4)$ if its ordered $[(CH_3)_2NH_2)]^+$ is removed, with this difference attributable to the missing linkers. The crystallographic data of Ho and Er members of the series also have additional weak reflections, consistent with the complete structure of these materials being a modulation of the one described here with a k-vector of [~1/3,0,0]. Attempts to solve the structure in a commensurate supercell in which the *a*-axis is tripled were unsuccessful, likely because the very weak intensities of these additional reflections do not provide enough information to stably refine this more complex structure or that the modulation is subtly incommensurate. Equivalent reflections were not seen in the data from Tb or Dy analogues.

Thermal Stability and Magnetic Properties

Thermal analysis of the samples indicate that all four phases are stable up to 290-300 °C. Above ~300 °C they decompose exothermically via what appears to be a poorly separated two-step process (see Figure S6). Below the decomposition temperature there is only minimal change in weight; this is consistent with the contents within the anionic framework not being readily removed from the structure, as would be expected if they were occupied by $[(CH_3)_2NH_2)]^+$.

Field cooled (FC) and zero field cooled (ZFC) measurements of A*Ln*$(HCO_2)(C_2O_4)_{1.5}$ samples were collected under a 1 kOe field. These indicated the compounds remained paramagnetic down to 2 K (see Figure 3). Consistent with this, good linear fits were obtained to plots of inverse susceptibility measurements for all compounds, broadly consistent with effective magnetic moments of 9.30, 9.82, 9.87 and 9.65 μ_B for the Tb, Dy, Ho and Er analogues, *c.f.* 9.72, 10.65, 10.61 and 9.58 μ_B expected from the Russel-Saunders coupling scheme (see Figure S7). These fits also yielded Weiss constants, Θ_W, of -4.33 K, -4.07 K, -6.50 K and -4.27 K for the Tb, Dy, Ho and Er compounds, respectively, consistent with antiferromagnetic interactions but it must be noted that there may be contributions to this from crystal field effects at low temperature. As all superexchange pathways between lanthanides in this structure are via *anti-anti* carboxylate bridges the suggested antiferromagnetic coupling is consistent with the previous work of Scatena *et al.*;[44] this showed that symmetric superexchange between occupied metal orbitals via *anti-anti* formate bridges favours antiferromagnetic coupling. Consistent with this $\chi_M T$ decreases on cooling, rapidly so for all materials below 60 K (see Figure 3). Isothermal magnetisation measurements at 2 K indicate magnetisation rises relatively rapidly up to about 10 kOe, above which they increase more slowly as they near saturation reaching maximum values of 4.55, 5.52, 4.78 and 5.36 μ_B for Tb, Dy, Ho and Er, respectively at 50 kOe (see Figure 4); these values are relatively close to *gJ*/2 consistent with Ising-like spins caused by the considerable orbital angular momentum and strong spin-orbit coupling of these lanthanides. There are no clear indications of hysteresis, consistent with paramagnetic behaviour.

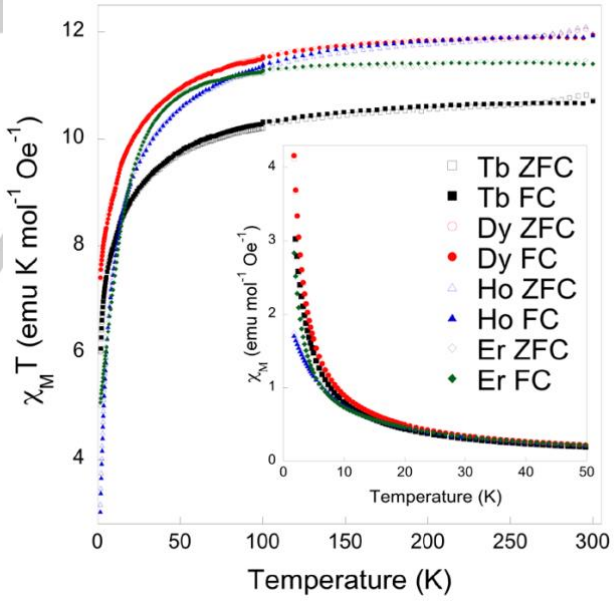

Figure 3. Plot of $\chi_M T$ of the A*Ln*$(HCO_2)(C_2O_4)_{1.5}$ phases as a function of temperature measured in a 1 kOe applied field with FC and ZFC measurements shown as filled and hollow symbols, respectively. Insert shows the change in χ_M below 50 K, confirming the retention of the paramagnetic state to 1.8 K.

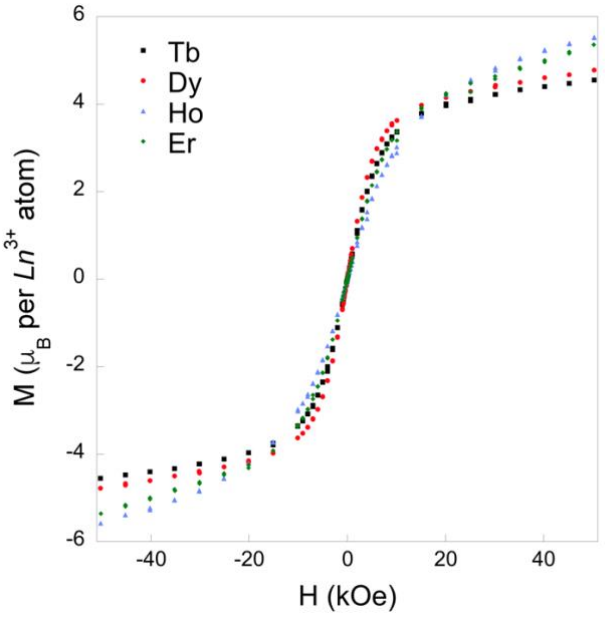

Figure 4. Isothermal magnetisation measurements of the A*Ln*$(HCO_2)(C_2O_4)_{1.5}$ phases at 2 K.

Conclusion

A family of A*Ln*$(HCO_2)(C_2O_4)_{1.5}$ phases have been synthesised solvothermally and found to be rare examples of perovskite-like hybrid materials with B^{3+} cations and ordered anion vacancies. The monovalent A-site cations required to charge balance the anionic frameworks are disordered preventing crystallographic identification. Infrared and neutron spectroscopies combined with elemental composition, however, clearly indicate the A-site cations are $[(CH_3)_2NH_2]^+$ molecules. This highlights the benefits of this complementary approach for identifying disordered species and the key importance of INS spectra in this due to its high sensitivity to R-H modes that are dominantly associated with molecular cations in hybrid perovskites. These compounds are found to be stable to about 300 °C, consistent with the pores of the frameworks being occupied by charged species. Magnetic property measurements suggest the frameworks have weak antiferromagnetic coupling.

Experimental Section

A$Tb(HCO_2)(C_2O_4)_{1.5}$, which is a white powder, was synthesised using $Tb(NO_3)_3{\cdot}5H_2O$ (4.5 mmol, 99.99+ %, Acros Organics) and oxalic acid (6.5 mmol, 98 %, Acros Organics) in DMF (39.1 ml, >99 %, Fisher Scientific) and heated at 150 °C for 48 hours in a 100 ml glass jar and Teflon lid. Pale yellow Dy and Ho analogues were synthesised using a similar approach but with $Dy(NO_3)_3{\cdot}5H_2O$ (4.3 mmol, 99.9 %, Alfa Aesar) or $Ho(NO_3)_3{\cdot}5H_2O$ (4.3 mmol, 99.9 %, Alfa Aesar) substituted for $Tb(NO_3)_3{\cdot}5H_2O$ and additional dimethylamine (2 mmol, 33 wt % in ethanol, Sigma Aldrich). A pale pink Er analogue was initially synthesised on a smaller scale, using a 25 mL jar, using $Er(NO_3)_3{\cdot}5H_2O$ (1.0 mmol, 99.9 % Acros Organics), oxalic acid (1.5 mmol) and dimethylamine solution (0.5 mmol); scaling this up to the same scale as the other compounds in this series was used for neutron characterisation. Good yields were obtained for all these products, 83.7 % for $[(CH_3)_2NH_2)]Tb(HCO_2)(C_2O_4)_{1.5}$ and between 92.2-94.1 % for the other analogues.

Single crystal structure determinations were carried out using a dual source Rigaku Oxford Diffraction Supernova utilising the Cu Kα micro-focus source (0.8 kV, 50 mA) with multi-layered focusing optics and an Atlas S2 CCD detector. Samples were cooled, when required, using an Oxford Cryosystems cryostream with samples held on MiTeGen micro loops. Data were integrated and absorption corrections performed using CrysAlisPro software suite version 171.38.41[45] using direct methods in SHELXS[46] or SHELXT[47] or charge density methods in olex.2[48] and least-squares refinements carried out using SHELXL-2014[49] via the Olex^2,[48] or in the case of the Tb analogue, APEX3 graphical user interface (GUI). Structures are deposited in the Cambridge Structural Database (CSD) as deposition numbers 2082806 & 2082807 (Tb phase), 208208 & 208209 (Dy phase), 208210 & 208211 (Ho phase) and 208212 & 208213 (Er phase)

Powder diffraction was used to assess sample purity and were collected using a Rigaku Miniflex utilising Cu Kα radiation (40 kV, 15mA) and D/teX Ultra detector. Patterns were collected in reflection geometry with the samples mounted on zero background Si wafer plates. Refinements were carried out using the Rietica software version 4.0[50]. Elemental microanalysis was carried out at the London Metropolitan University. Infrared spectra were measured between 500 and 4000 cm^{-1} using a Shimadzu IRAffinity-1S Fourier Transform Spectrometer equipped with an attenuated total reflection stage. Measurements were averaged over 32 scans with a resolution of 4 cm^{-1}. Neutron spectroscopy measurements were collected from A$Er(HCO_2)(C_2O_4)_{1.5}$ on the INS spectrometer TOSCA on TS1 at ISIS at the Rutherford Appleton Laboratories, Oxford[51,52] This measurement was performed at 10 K using an aluminium cell and the spectrum collected over a 3 hour scan.

TGA-DSC was carried out simultaneously using a NETZSCH 409 PG/PC TGA. The sample was held in a ceramic crucible and heated under flowing N_2 at a rate of 10 or 20°/minute from about 25 °C to 600 °C. Direct Current (DC) SQUID measurements were collected using Quantum Design's Magnetic Property Measurement System (MPMS) using the MPMS MultiVu Application with the sample mounted in a straw with a uniform diamagnetic background. Field-cooled (FC) and zero field-cooled (ZFC) measurements were taken, using an applied field of 1 kOe between 2 K and 300 K with isothermal magnetisation measurements obtained at 2 K under fields of up to 50 kOe.

Acknowledgements

We would like to thank Engineering and Physical Sciences Research Council for funding via project EP/R011524/1. Experiments at the ISIS Pulsed Neutron and Muon Source were supported by an Xpress beamtime allocation from the Science and Technology Facilities Council.

Keywords: Crystal Engineering • Lanthanides • Metal-organic frameworks • Neutron spectroscopy • Perovskite phases

[1] J. B. Goodenough, *Reports Prog. Phys.* **2004**, *67*, 1915–1993.
[2] B. Raveau, A. Maignan, C. Martin, M. Hervieu, *Chem. Mater.* **1998**, *10*, 2641–2652.
[3] C. Moure, O. Peña, *Prog. Solid State Chem.* **2015**, *43*, 123–148.
[4] M. Kubicek, A. H. Bork, J. L. M. Rupp, *J. Mater. Chem. A* **2017**, *5*, 11983–12000.
[5] R. H. Mitchell, *Perovskites: Modern and Ancient*, Almaz Press, Thunder Bay, Ontario, **2002**.
[6] C. J. Howard, Z. Zhang, *J. Phys. Condens. Matter* **2003**, *15*, 4543–4553.
[7] Q. Zhou, P. J. Saines, N. Sharma, J. Ting, B. J. Kennedy, Z. Zhang,

R. L. Withers, K. S. Wallwork, *Chem. Mater.* **2008**, *20*, 6666–6676.
[8] W. Li, Z. Wang, F. Deschler, S. Gao, R. H. Friend, A. K. Cheetham, *Nat. Rev. Mater.* **2017**, *2*, 16099.
[9] Z. Wang, K. Hu, S. Gao, H. Kobayashi, *Adv. Mater.* **2010**, *22*, 1526–1533.
[10] G. Rogez, N. Viart, M. Drillon, *Angew. Chemie Int. Ed.* **2010**, *49*, 1921–1923.
[11] W.-J. Xu, S. Kopyl, A. Kholkin, J. Rocha, *Coord. Chem. Rev.* **2019**, *387*, 398–414.
[12] H. S. Jung, N.-G. Park, *Small* **2015**, *11*, 10–25.
[13] S. D. Stranks, H. J. Snaith, *Nat. Nanotechnol.* **2015**, *10*, 391–402.
[14] B. Saparov, D. B. Mitzi, *Chem. Rev.* **2016**, *116*, 4558–4596.
[15] Y. Wu, T. Binford, J. A. Hill, S. Shaker, J. Wang, A. K. Cheetham, *Chem. Commun.* **2018**, *54*, 3751–3754.
[16] X.-H. Zhao, X.-C. Huang, S.-L. Zhang, D. Shao, H.-Y. Wei, X.-Y. Wang, *J. Am. Chem. Soc.* **2013**, *135*, 16006–16009.
[17] L. C. Gómez-Aguirre, B. Pato-Doldán, A. Stroppa, L.-M. Yang, T. Frauenheim, J. Mira, S. Yáñez-Vilar, R. Artiaga, S. Castro-García, M. Sánchez-Andújar, M. A. Señarís-Rodríguez, *Chem. – A Eur. J.* **2016**, *22*, 7863–7870.
[18] S. M. Bovill, P. J. Saines, *CrystEngComm* **2015**, *17*, 8319–8326.
[19] A. Cornia, A. Caneschi, P. Dapporto, A. C. Fabretti, D. Gatteschi, W. Malavasi, C. Sangregorio, R. Sessoli, *Angew. Chemie Int. Ed.* **1999**, *38*, 1780–1782.
[20] Y.-Q. Tian, Y.-M. Zhao, H.-J. Xu, C.-Y. Chi, *Inorg. Chem.* **2007**, *46*, 1612–1616.
[21] P. Samarasekere, X. Wang, W. Kaveevivitchai, A. J. Jacobson, *Cryst. Growth Des.* **2015**, *15*, 1119–1128.
[22] W. Yao, Y.-Y. Guo, P. Lightfoot, *Dalton Trans.* **2017**, *46*, 13349–13351.
[23] R. Clulow, A. J. Bradford, S. L. Lee, P. Lightfoot, *Dalton Trans.* **2019**, *48*, 14461–14466.
[24] H. He, W. Yao, S. Tunmee, X. Zhou, B. Ji, N. Wu, T. Song, P. Kidkhunthod, Y. Tang, *J. Mater. Chem. A* **2020**, *8*, 9128–9136.
[25] X. He, X. Zhang, B. Ji, W. Yao, P. Lightfoot, Y. Tang, *Chem. Commun.* **2021**, *57*, 2567–2570.
[26] L. G. Burley, J. Beecham-Lonsdale, A. K. Srivastava, I. E. Collings, P. J. Saines, *Dalton Trans.* **2021**, *50*, 5437–5441.
[27] V. A. Blatov, A. P. Shevchenko, D. M. Proserpio, *Cryst. Growth Des.* **2014**, *14*, 3576–3586.
[28] "The Samara Topological Data Center," can be found under https://topcryst.com/, **2021.**
[29] H. A. Evans, Y. Wu, R. Seshadri, A. K. Cheetham, *Nat. Rev. Mater.* **2020**, *5*, 196–213.
[30] I. Spanopoulos, W. Ke, C. C. Stoumpos, E. C. Schueller, O. Y. Kontsevoi, R. Seshadri, M. G. Kanatzidis, *J. Am. Chem. Soc.* **2018**, *140*, 5728–5742.
[31] A. Senocrate, I. Spanopoulos, N. Zibouche, J. Maier, M. S. Islam, M. G. Kanatzidis, *Chem. Mater.* **2021**, *33*, 719–726.
[32] A. E. Fedorovskiy, N. A. Drigo, M. K. Nazeeruddin, *Small Methods* **2020**, *4*, 1900426.
[33] P. Vishnoi, J. L. Zuo, T. A. Strom, G. Wu, S. D. Wilson, R. Seshadri, A. K. Cheetham, *Angew. Chemie Int. Ed.* **2020**, *59*, 8974–8981.
[34] A. L. Spek, *Acta Crystallogr. Sect. C* **2015**, *71*, 9–18.
[35] A. Trzesowska, R. Kruszynski, T. J. Bartczak, *Acta Crystallogr. Sect. B* **2004**, *60*, 174–178.
[36] K. Esperdy, D. D. Shillady, *J. Chem. Inf. Comput. Sci.* **2001**, *41*, 1547–1552.
[37] H. He, Y. Zhang, W. Zhu, A. Zheng, *Mater. Res. Bull.* **2011**, *46*, 1546–1552.
[38] D. C. Palmer, *Zeitschrift für Krist. - Cryst. Mater.* **2015**, *230*, 559–572.
[39] N. L. Allinger, Y. H. Yuh, J. H. Lii, *J. Am. Chem. Soc.* **1989**, *111*, 8551–8566.
[40] J.-H. Lii, N. L. Allinger, *J. Comput. Chem.* **1991**, *12*, 186–199.
[41] D. E. Williams, *J. Comput. Chem.* **2001**, *22*, 1154–1166.
[42] A. K. Rappe, C. J. Casewit, K. S. Colwell, W. A. Goddard, W. M. Skiff, *J. Am. Chem. Soc.* **1992**, *114*, 10024–10035.
[43] C. F. Macrae, I. Sovago, S. J. Cottrell, P. T. A. Galek, P. McCabe, E. Pidcock, M. Platings, G. P. Shields, J. S. Stevens, M. Towler, P. A. Wood, *J. Appl. Crystallogr.* **2020**, *53*, 226–235.
[44] R. Scatena, R. D. Johnson, P. Manuel, P. Macchi, *J. Mater. Chem. C* **2020**, *8*, 12840–12847.
[45] CrysAliPro Software system, version 1.171.38.43, Rigaku Oxford Diffraction, **2018**.
[46] G. M. Sheldrick, *Acta Crystallogr. Sect. A* **2008**, *64*, 112–122.
[47] G. M. Sheldrick, *Acta Crystallogr. Sect. A* **2015**, *71*, 3–8.
[48] O. V Dolomanov, L. J. Bourhis, R. J. Gildea, J. A. K. Howard, H. Puschmann, *J. Appl. Crystallogr.* **2009**, *42*, 339–341.
[49] G. M. Sheldrick, *Acta Crystallogr. Sect. C* **2015**, *71*, 3–8.
[50] B. A. Hunter, C. J. Howard, *A Computer Program for Rietveld Analysis of X-Ray and Neutron Powder Diffraction Patterns*, **1998**.
[51] D. Colognesi, M. Celli, F. Cilloco, R. J. Newport, S. F. Parker, V. Rossi-Albertini, F. Sacchetti, J. Tomkinson, M. Zoppi, *Appl. Phys. A* **2002**, *74*, s64–s66.
[52] R. S. Pinna, S. Rudić, S. F. Parker, J. Armstrong, M. Zanetti, G. Škoro, S. P. Waller, D. Zacek, C. A. Smith, M. J. Capstick, D. J. McPhail, D. E. Pooley, G. D. Howells, G. Gorini, F. Fernandez-Alonso, *Nucl. Instruments Methods Phys. Res. Sect. A Accel. Spectrometers, Detect. Assoc. Equip.* **2018**, *896*, 68–74.

Entry for the Table of Contents

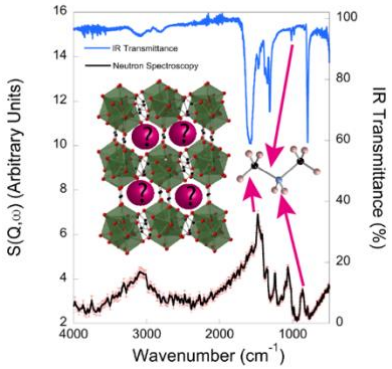

Hybrid perovskite-like A*Ln*$(HCO_2)(C_2O_4)_{1.5}$ phases have a mixture of monovalent and divalent ligands, supporting an unusual combination of A^+ and B^{2+} cations along with ordered anion vacancies. The disordered A-site cations cannot be resolved crystallographically but are clearly identified as $[(CH_3)_2NH_2]^+$ using a combination of neutron and infrared spectroscopy.

Institute and/or researcher Twitter usernames: @saines_408